Influence of focus offset on the microstructure of an intermetallic gamma-TiAl based alloy produced by electron beam powder bed fusion

Journal of Manufacturing Processes 89 (2023) 132–141

Contents lists available at ScienceDirect

Journal of Manufacturing Processes

journal homepage: www.elsevier.com/locate/manpro

Influence of focus offset on the microstructure of an intermetallic γ-TiAl based alloy produced by electron beam powder bed fusion

C. Ghibaudo [a,b,c,*], R. Wartbichler [d], G. Marchese [a,b,c], H. Clemens [d], D. Ugues [a,b,c], S. Biamino [a,b,c]

[a] Department of Applied Science and Technology, Politecnico di Torino, Corso Duca degli Abruzzi 24, 10129 Torino, Italy
[b] Center of Integrated Additive Manufacturing (IAM), Politecnico di Torino, Corso Castelfidardo 51, 10129 Torino, Italy
[c] Consorzio Interuniversitario Nazionale per la Scienza e Tecnologia dei Materiali-INSTM, Italy
[d] Department of Materials Science, Montanuniversität Leoben, Franz-Josef-Str. 18, A-8700 Leoben, Austria

ARTICLE INFO

Keywords:
Additive manufacturing
electron beam powder bed fusion
Focus offset
Intermetallics
Titanium aluminides

ABSTRACT

It is well established in literature that, when processing intermetallic γ-TiAl components by electron beam powder bed fusion, a banded microstructure is frequently formed because of an inhomogeneous Al distribution since more pronounced evaporation of Al occurs at the top of the melt pool.

This feature is particularly promoted when highly energetic process parameters (high beam currents, slow beam speeds, narrow line offsets) are used. Therefore, an approach already suggested in the literature to reduce the Al loss is to minimize the energy level of the process parameter during production. However, there is a limit to such kind of approach: minimizing the beam current or increasing the beam speed, or increasing the line offset will, at a certain point, results in not being able to achieve a completely dense material and thus some process-induced porosity, the so-called lack-of-fusion defects, starts to occur in the produced parts.

In this study, the effect of an additional parameter of the electron beam powder bed fusion process is taken under consideration: the focus offset (FO), i.e. the distance between the focusing plane of the electron beam with respect to the powder bed. The effect of the FO on the residual porosity, microstructure, phase composition, hardness as well as chemical composition is investigated, thus having the possibility to demonstrate that also the FO can affect the Al loss and play a fundamental role in the generation of a homogenous microstructure, contributing to mitigate the appearance of a banded microstructure.

1. Introduction

Intermetallic γ-TiAl-based alloys are interesting structural materials because of their low density (around 4 g/cm^3) and outstanding properties, such as high specific tensile strength, high specific Young's modulus as well as excellent creep resistance for components working at elevated temperatures (600–750 °C), especially when compared with the heavier (about 8 g/cm^3) Ni-base superalloys [1–6]. For instance, in 2006, GE announced the implementation of the γ-Ti-48Al-2Nb-2Cr alloy (in at.%, unless stated otherwise) for low-pressure turbine (LPT) blades for the 6th and 7th stages of the GEnx™-1B aircraft engines powering the Boeing 787 aircraft [7]. The utilization of TiAl alloys allows the reduction of fuel consumption, NO_X emissions, and noise when compared with former engines [8]. Intermetallic γ-TiAl-based alloys also find application in the automotive sector, where they are employed as the constituent material for turbine wheels in turbochargers to increase engine efficiency and decrease harmful emissions. An example can be found in the Lancer cars model of Mitsubishi, which is equipped with a γ-TiAl turbocharger [9]. Furthermore, at the beginning of the late 1990s, in Formula 1 racing engines, the use of γ-TiAl-based alloys as valve material was revolutionary and provided a significant performance advantage that has fundamentally changed the engine designer's concept for light and heat-resistant valves [10].

The good mechanical properties of γ-TiAl based alloys stem from their microstructures and constituent phases [4,11,12]. The main constituent phases are the γ-TiAl phase ($L1_0$ ordered tetragonal face-centered structure) and the α_2-Ti_3Al phase ($D0_{19}$ ordered hexagonal structure). Moreover, it is possible to find traces of β_0-phase (B2 ordered body-centered structure) [8,13,14]. The general mechanical properties associated with the respective microstructure are reported in the work of

* Corresponding author at: Department of Applied Science and Technology, Politecnico di Torino, Corso Duca degli Abruzzi 24, 10129 Torino, Italy.
E-mail address: cristian.ghibaudo@polito.it (C. Ghibaudo).

https://doi.org/10.1016/j.jmapro.2023.01.061
Received 14 September 2022; Received in revised form 12 December 2022; Accepted 23 January 2023
Available online 2 February 2023

Recina et al. [15]. The microstructures of γ-TiAl-based alloys are commonly divided into four types: i) fully lamellar, ii) nearly lamellar, iii) duplex, and iv) equiaxed. The lamellar grains are responsible for high creep resistance and toughness, although a high amount of lamellar colonies is detrimental to ductility at room temperature and to fatigue resistance. On the contrary, the equiaxed microstructure enables the improvement of the ductility at room temperature as well as fatigue resistance [3,4,8,15,16]. For this reason, the desired microstructure must be carefully tailored for the envisaged structural component through the optimization of both its processing route and its subsequent heat treatment, thus matching the mechanical properties required for its application.

At present, the state of art for the production of γ-TiAl-based alloy components such as LPT blades is precision casting, despite some issues [4,11,12,16]. Firstly, the crucible used in the casting process may be the source of possible contaminations, and this is particularly critical in the case of γ-TiAl-based alloys due to their high reactivity in the melted state [17]. In particular, if the oxygen content exceeds 0.1 wt%, the plastic fracture strain under tensile loading, that it is known not to be very high for these alloys and it is always the critical point to face for their industrial applications, is drastically reduced [4]. Secondly, preheated moulds are necessary to avoid an incomplete filling due to the high viscosity of the melt, thus resulting in a slow cooling rate and thus to the formation of a coarser microstructure or segregation of the heavier alloying elements.

Thanks to the possibility of overcoming the above mentioned casting drawbacks, electron beam-powder bed fusion (EB-PBF) started to be considered a very attractive additive manufacturing technique to process γ-TiAl-based alloys. The high preheating temperature, i.e. over the brittle-to-ductile transition temperature of TiAl alloys (around 700 °C), allows the production of crack-free components, while the controlled vacuum (2×10^{-3} mbar, adjusted by backfilling He flux) limits concentration of interstitial elements in the component [18–21]. So, since 2010, the processability of γ-TiAl-based alloys by EB-PBF has been studied, where the initial works of Biamino et al. [19] and Murr et al. [20] have mainly paid attention to the achievement of dense samples and components. More details on the process steps of EB-PBF can be found in [22,23].

However, the vacuum environment and the high local energy employed in the EB-PBF process lead to easy evaporation of some light elements, for example, Al in γ-TiAl-based alloys. This Al evaporation occurs from the top of the melt pool, so if it is not controlled, it may generate a banded microstructure consisting of alternating Al-depleted zones and Al-rich zones as reported in [13,18,24–26]. For γ-TiAl-based alloys, this microstructure feature is typical of the EB-PBF process, and the response in terms of mechanical properties was, for instance, studied by Todai et al. [26] resulting in a high anisotropy of the tensile properties. Such high anisotropy in the tensile properties is caused by the preferential orientation (perpendicularly to the building direction) of the banded microstructure originated by a not homogeneous Al evaporation. No anisotropy caused by the solidification direction in each layer or due to the thermal gradient in the building direction have ever been reported for γ-TiAl-based alloys processed by EB-PBF. This behavior is different than observed in Ni-superalloys [27,28] or Ti alloys [29] where, in the as-built condition, grains are typically elongated in the building direction due to the thermal gradient in the building direction.

Regarding the EB-PBF process parameters, there are already investigations that deal with the effect of the current, the speed, and the line offset of the electron beam on the Al loss, proposing the reduction of the energy input given to the material as a route to limit the Al loss, thus increasing the microstructural homogeneity [11,15,22]. However, it was already reported that low energy densities can lead to not complete densification of the built specimens with process-related residual porosities, the so-called lack-of-fusion (LoF) defects [25,30–32].

Despite the various studies on the effect of the process parameters on the processability of γ-TiAl-based alloys, there is a parameter whose role in Al loss and microstructure modification has never been investigated so far: the focus offset (FO). The FO is a current that shifts the focal plane, thus modifying the dimensions of the electron beam spot size on the powder bed [33–37]. So, the present paper aims to study the effect of the FO on the residual porosity, microstructure, chemical composition, phases, and hardness using a Ti-48Al-2Nb-2Cr alloy. Furthermore, subsequent heat treatments were performed to compare the microstructure evolution of samples produced with two different FOs.

Table 1
Chemical composition (in atomic percentage, at.%) of the starting powder determined by OES-ICP analysis.

	Al	Cr	Nb	Fe	Ti
Powder	48.73	1.92	2.00	0.03	Bal.

2. Materials and methods

In this study, gas atomized Ti-48Al-2Nb-2Cr powder with particle sizes between 40 and 150 μm was supplied by Arcam EBM (GE Additive). Table 1 lists the chemical composition of the powder determined through optical emission spectrometer-inductively coupled plasma (OES-ICP) analysis.

Cuboid samples with a side of 18 mm and a height of 35 mm were built using an A2X Arcam EBM (GE Additive) machine at an accelerating voltage of 60 kV. The melting parameters were kept constant (beam current, $I = 10$ mA, beam speed, $v = 1600$ mm/s, line offset, $L_{off} = 0.2$ mm), except for the FO, varied from 5 to 30 mA. The samples will be hereafter identified by the FO used, where the value of the current, expressed in mA, will be reported as a subscript (example: FO_{+5} means that a current of 5 mA was used for the FO parameter). A scanning strategy with a rotation of 90° between consecutive layers was used. A preheating temperature of 1050 °C was set using the defocused beam atop each newly spread powder layer of 90 μm during the preheating step. The preheating temperature was measured by a thermocouple located below the building platform, and, consequently, the registered temperature slightly decreased to around 1010 °C when reaching a total height of 35 mm.

For metallographic preparation, the samples were cut along the building direction and ground using SiC sandpapers up to 2500 grit. Finally, the samples were polished down to 0.03 μm with OP-S suspension. The polished samples were analyzed to determine the residual porosity by means of a light optical microscope (LOM, Zeiss AXIO Imager.M2 equipped with an Axio-CamHRc.5 camera). A total of 20 LOM images per sample at 50× were taken and subsequently post-processed with ImageJ software. For the microstructural analyses, a scanning electron microscope (SEM Versa 3D Dual Beam from Thermo Fischer, formerly FEI, operating at 10 kV) was used in backscattered electron (BSE) mode. In all the micrographs, the building direction Z is upwards.

In order to evaluate the mechanical performance, Vickers hardness tests HV0.05 and HV10 were carried out on polished samples using a Qness 60 A+ microhardness tester from ATM Qness. The Vickers hardness was conducted with 10 indentations per sample. Moreover, for some selected conditions, a micro Vickers hardness map was produced by executing 900 indentations (30 × 30 with a distance of 50 μm between each indentation), covering an area of 1.5×1.5 mm^2.

X-Ray Diffraction (XRD) analyses were performed on the samples to quantitatively determine the phases by Rietveld refinement using TOPAS 4.1 software. XRD analyses were performed utilizing a D8 Advanced diffractometer from Bruker AXS, using Cu-K_α radiation and an angular range of 11–82° with a step size of 0.02° in a Bragg-Brentano geometry.

Thermomechanical analysis (TMA - Setaram Setsys Evolution) was performed on $5 \times 5 \times 10$ mm^3 samples extracted from the $18 \times 18 \times 35$

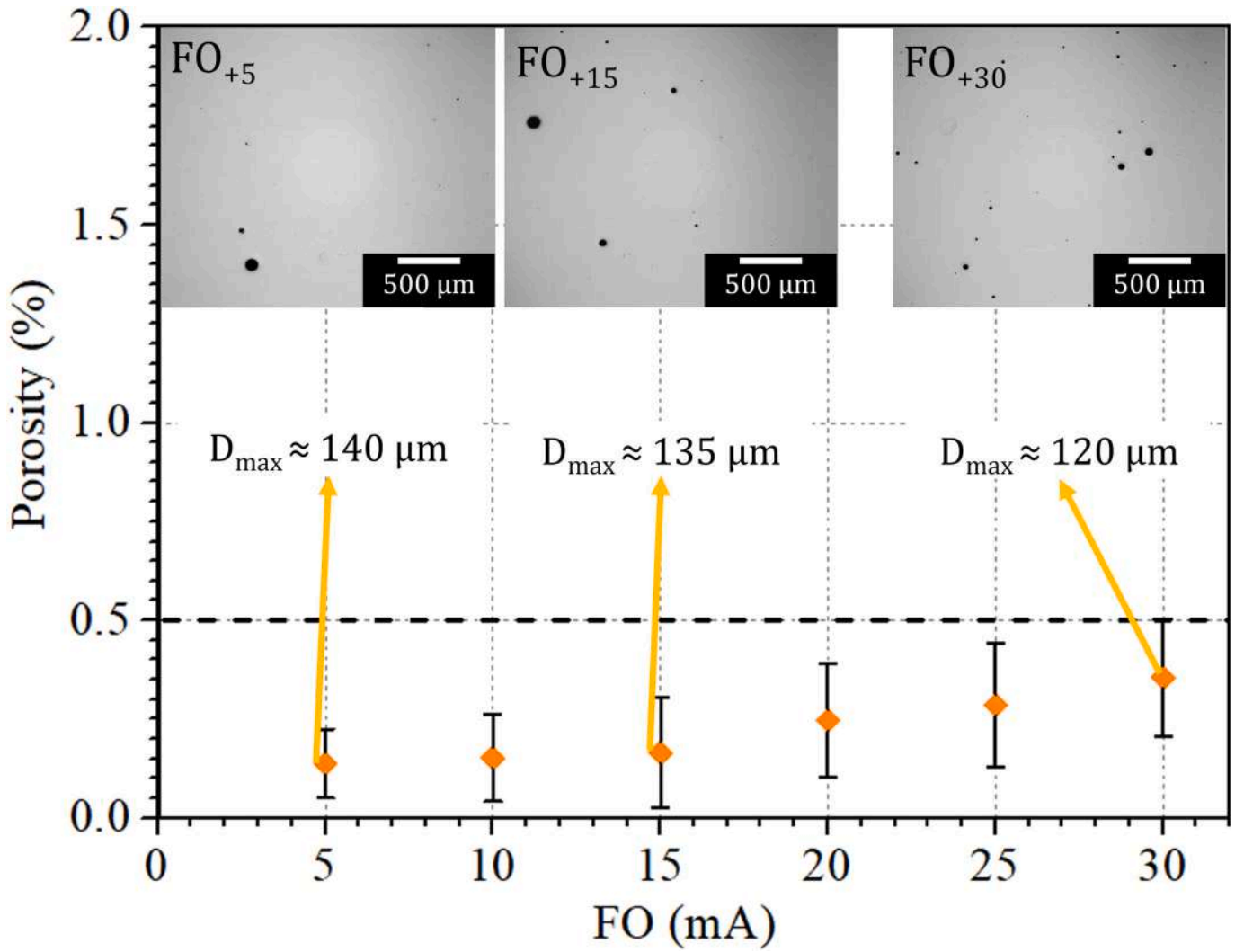

Fig. 1. Residual porosity of the samples built using different FOs. LOM images showing the residual defects of the samples FO_{+5}, FO_{+15}, and FO_{+30} with the maximum diameter (D_{max}) of the detected circular pore.

mm^3 specimens produced with different FOs. TMA was used to determine the phase transition temperatures in the range of 1250 and 1400 °C using a heating rate of 5 °C/min under an Ar flow of 20 ml/min to prevent oxidation. The chemical content of selected specimens was obtained by X-ray fluorescence (XRF) analysis.

Afterward, two conditions with low (FO_{+5}) and high FO (FO_{+30}) were subjected to subsequent heat treatments to compare their microstructure evolution.

These samples were heat-treated at 1050 °C for 24 h followed by air cooling and then analyzed by means of electron backscattered diffraction (EBSD using FEI system) to evaluate the distribution of the phases and their morphology. The samples were vibro-polished for 1 h using 0.03 µm OP-S suspension. The analysis was carried out at 30 kV with a spot size of 7 µm and a step size of 500–1000 nm. The software Team 4.3 and TSL OIM Analysis 7 were employed for performing the measurement. Considering that literature reports the challenge to properly detect γ-TiAl as a tetragonal phase due to the c/a ratio close to 1, γ-TiAl phase was measured as a cubic phase [13,38,39].

Moreover, the microstructure of the heat-treated samples at 1310 °C for 2 h followed by a cooling rate of around 125 °C/min was characterized by means of SEM in order to compare the generated microstructure from two different FOs.

Finally, the phases' transformation was observed and recorded using a laser scanning confocal microscope (LSCM, VL2000DX-SVF17SP Yonekura HT) under heating at high temperature and then cooling down to room temperature. The heating parameters for the LSCM were selected to generate a duplex microstructure. The parameters were: i) from 100 to 1100 °C heating with 500 °C/min, ii) from 1100 to 1310 °C with a heating rate of 50 °C/min in order to observe the eutectoid phase transition $\alpha_2 + \gamma \rightarrow \alpha + \gamma$, iii) isotherm at 1310 °C for 10 min, iv) cooling down to 1000 °C with a cooling rate of 100 °C/min to observe the lamellar precipitation, and v) finally a fast cooling down to room temperature. A flow of Ar prevented the oxidation of the sample during all the steps.

3. Results and discussion

Fig. 1 shows that, regarding the experimental conditions investigated in this paper, the porosity grew only marginally with the increment of the FO and was always below 0.5 %, which is a value in the same range reported in the literature for other γ-TiAl alloys [40–42]. Looking at the cross-sections of all the specimens, only scattered circular pores with diameters always less than 150 µm have been identified and can be in the insert of Fig. 1.

However, the authors would like to point out that this finding is factual only for the present experimental conditions. Nevertheless, more important changes of the FO or investigating different I and v conditions or different materials than TiAl alloys it may happen that FO changes do

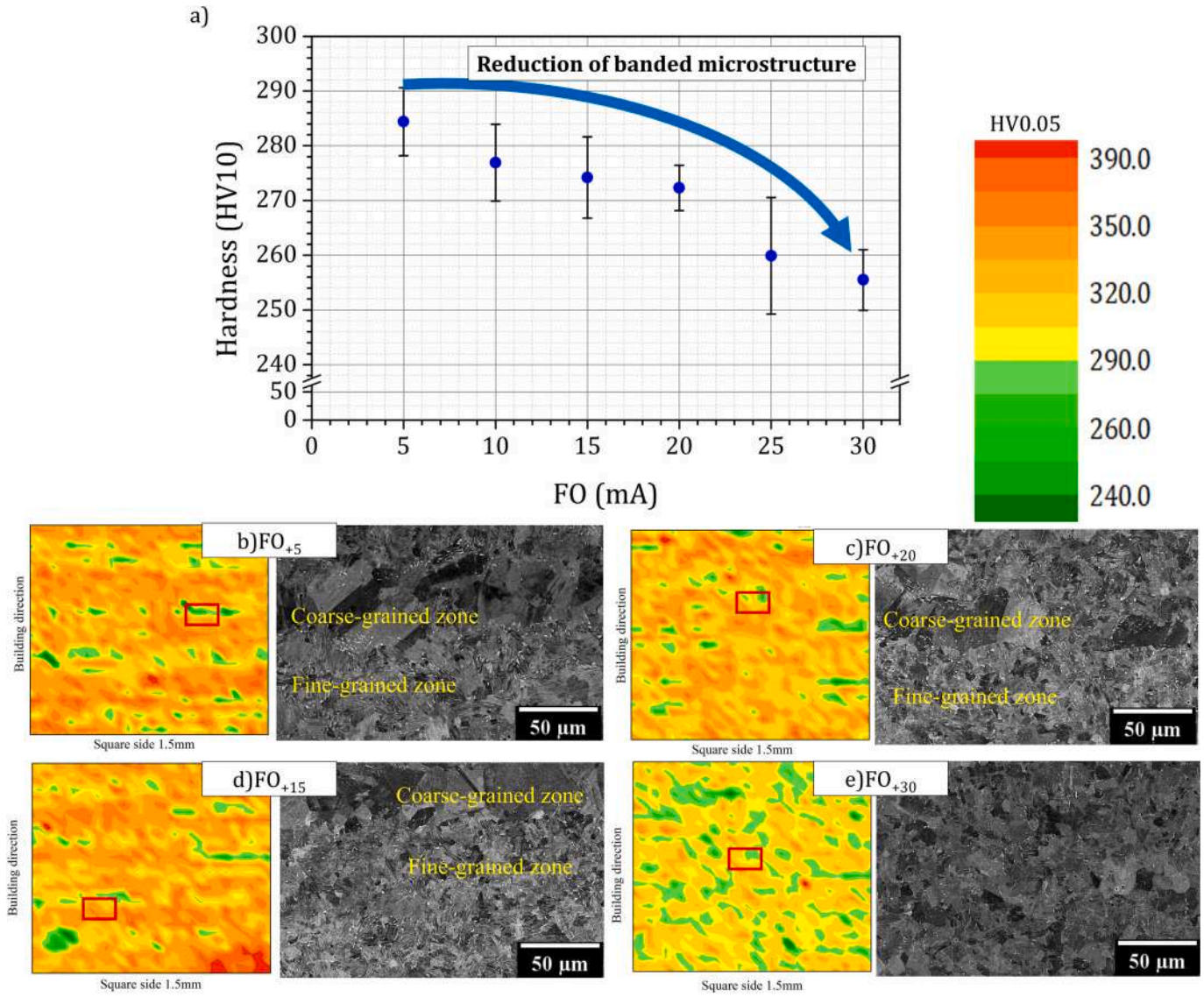

Fig. 2. a) HV10 hardness of samples produced with different FOs; b-e) HV0.05 maps reporting the microhardness distribution with a SEM image at high magnification showing the presence or absence of banded structures. The SEM-BSE micrographs represent the areas pointed out by the red rectangle on the HV0.05 maps. (For interpretation of the references to colour in this figure legend, the reader is referred to the web version of this article.)

play a decisive role in residual porosity. For instance, Lee et al. [35] reported the effect of the FO on the Inconel 718 alloy produced by EB-PBF. They observed that a highly defocused beam above a certain FO threshold involved the formation of LoF defects. Indeed, increasing the FO increases the beam spot size and the melt pool size. A wider and shallower melt pool size (with the same process parameters) means that the same energy is distributed on a larger area, thus reducing the energy input per area delivered into the melt pool. Consequently, too low area energies can result in a high level of process-derived LoF defects.

However, no LoF defects were detected for all the investigated samples, indicating that a variation of FO from 5 to 30 mA still allowed, at the actual I and v conditions, the production of specimens without large irregular porosities that can be referred to as process-induced defects, thus confirming that all the investigated FOs are eligible for successful production of specimens.

Afterward, the variation of the HV10 with the different FOs employed was characterized, and it is provided in the upper part of Fig. 2. An increment of the FO involved a gradual hardness reduction from FO_{+5} to FO_{+30}. In order to better investigate this aspect, similarly to what was done in a previous paper [13], a mapping of the hardness HV 0.05 distribution of the samples produced with various FOs was conducted and is displayed in the bottom part of Fig. 2, coupled with a SEM micrograph.

The sample with FO_{+5} exhibited a remarkable banded microstructure made of fine-grained zone alternated with coarse-grained ones. These two interpenetrating microstructures are not a novelty for γ-TiAl based alloy processed by EB-PBF and were deeply investigated in a previous paper [13]. The fine-grained zones developed from an Al-depleted region are constituted of a fine duplex-like microstructure to small lamellar colonies where the accumulation of the α_2-Ti_3Al phase exhibited a Zener pinning effect, thus inhibiting grain growth [43,44]. The grains are fine and there is this accumulation of α_2-Ti_3Al phase, which generally is harder than γ-TiAl phase in the Ti-48Al-2Cr-2Nb alloy [45] Therefore, these bands exhibited a higher hardness with respect to the coarse-grained zones, as confirmed by the hardness maps in the bottom part of Fig. 2.

A similar degree of banded microstructure could also be detected for FO_{+15} and FO_{+20} conditions. In contrast, the FO_{+30} specimen was characterized by a more homogenous microstructure and the corresponding hardness map that did not show banded structures. In

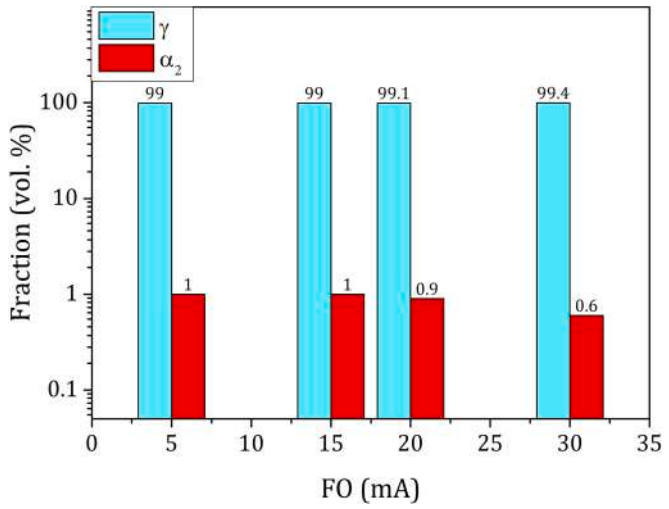

Fig. 3. Results of Rietveld phase quantification for Ti-48Al-2Cr-2Nb samples produced with different FOs.

particular, the fine-grained zones were severely reduced in the resulting microstructure of the FO_{+30} specimen, thus determining a general decrease in the overall hardness (see the upper part of Fig. 2).

The phase quantification using the Rietveld method performed on the samples (Fig. 3) confirmed that an increment of the FO involved a gradual reduction of α_2-phase content from FO_{+5} to FO_{+30}.

Since α_2-phase may be underestimated by XRD analysis due to its small dimensions, the extreme conditions (FO_{+5} and FO_{+30}) were heat-treated at 1050 °C for 24 h. Subsequently, the specimens were cut and XRD measurements were performed. This temperature is well below any transformation temperature of the material, so the heat treatment just increased the dimensions of the α_2-phase without altering the banded structures of the FO_{+5} sample (Fig. 4.a and b) or the more homogeneous microstructure of the FO_{+30} sample (Fig. 4.c and d) thus allowing the possibility to measure α_2 content by means of EBSD analysis.

In the EBSD analysis, the high-angle grain boundaries (HAGBs) are indicated by black lines, while the α_2 and γ-phases are identified by red and light blue, respectively, The lower α_2 content for FO_{+30} is confirmed clearly.

The Al-depleted regions that cause the banded structures are caused by a zone-by-zone differentiated Al evaporation. In particular, more pronounced evaporation of Al is revealed at the top of the melt pool, thus leading to inhomogeneous content of α_2-grains, which lock the grain growth of the γ-grains where there is an α_2 accumulation [13,25]. This feature is particularly marked when highly energetic process parameters (high beam currents, slow beam speeds, and narrow line offsets) are used [25,46]. However, this feature can also be influenced by the FO, as demonstrated by the current work.

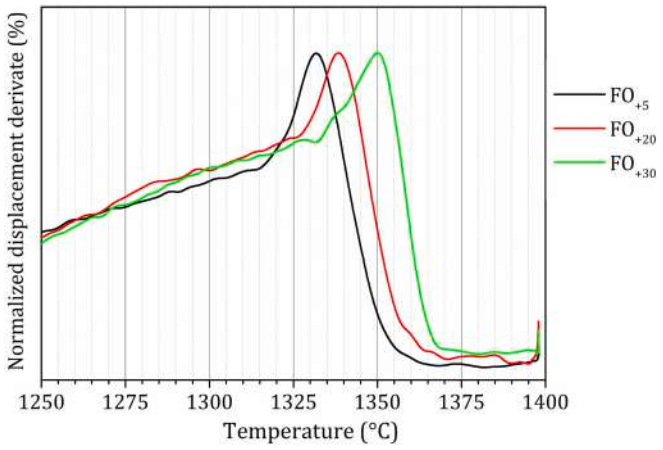

Fig. 5. Normalized displacement derivative curve over the temperature for samples produced with different FOs. The peaks indicate the α-transus temperature, see text.

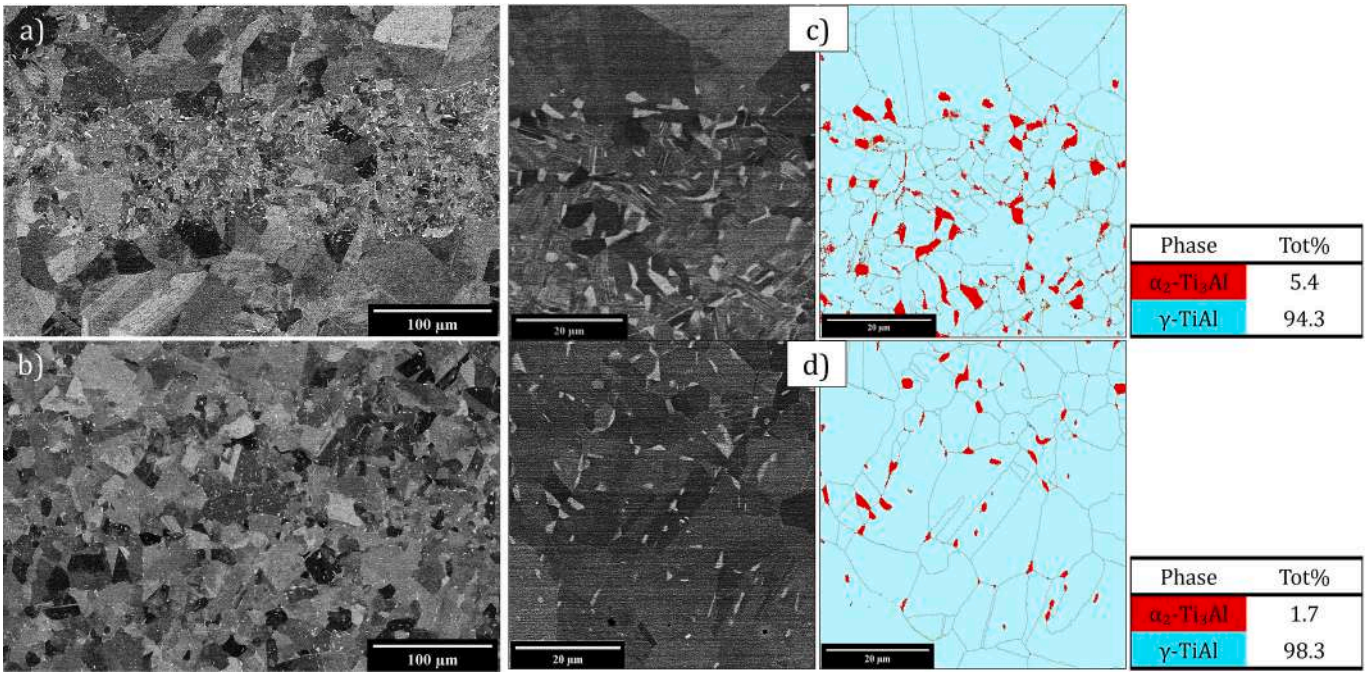

Fig. 4. SEM-EBSD images of samples heat-treated at 1050 °C for 24 h: a) low magnification view of the sample FO_{+5}; b) SEM and EBSD phase map of sample FO_{+5}; (c) low magnification view of the sample FO_{+30}; d) SEM and EBSD phase map of sample FO_{+30}. Note that in the EBSD phase maps, the HAGBs are indicated by black lines, while the γ-TiAl phase and the α_2-Ti_3Al phase are indicated in light blue and red, respectively. (For interpretation of the references to colour in this figure legend, the reader is referred to the web version of this article.)

Table 2
Chemical compositions (at.%) of the powder and bulk samples as determined by OES-IPC and XRF methods. The Al loss (at.%) for the bulk specimens was obtained by subtracting the Al value of the powder.

Sample	Al	Cr	Nb	Ti	Al loss
Powder	48.73	1.92	2.00	Bal.	–
FO_{+5}	47.48	1.92	2.03	Bal.	1.25
FO_{+20}	47.60	1.95	2.02	Bal.	1.13
FO_{+30}	48.04	1.95	1.99	Bal.	0.69

Consequently, it was also important to investigate the effects of the FOs on the Al evaporation. For this reason, both TMA and XRF chemical analyses were performed on the FO_{+5}, FO_{+20}, and FO_{+30} conditions. The derivate of the displacement of the different samples determined by TMA is shown in Fig. 5. The peak identified the α-transus temperature (T_α -$\alpha + \gamma \rightarrow \alpha$) [47], which resulted to be influenced by the FO. In detail, the T_α was 1332 °C, 1339 °C, and 1350 °C for FO_{+5}, FO_{+20}, and FO_{+30}, respectively.

These results were confirmed by the XRF analysis (Table 2), where gradual mitigation of the Al evaporation with the increment of the FO was measured. In detail, comparing the Al content of the powder with the samples produced at different FOs, an Al loss of 1.25 and 0.69 at.% occurred at FO_{+5} and FO_{+30}, respectively, thus confirming that by changing the FO it is possible to modify the distribution of the energy density.

3.1. Correlation of the focus offset with the porosity, microstructure, Al loss, and hardness

The increment of the FO enlarges the spot size following a parabolic trend that is influenced by the beam current used during the process. The machine suppliers did not completely disclose such kind of relationship, however, the only information we were able to find in literature about this topic, is the paper of Wadea et al. [33], in which the following equation in order to calculate the beam spot size from the FO was reported.

$$D_{beam} = 0.000102(FO)^2 + 0.00151(FO) + 0.131, \quad (1)$$

where D_{beam} is the diameter of the electron beam spot size in mm.

Fig. 6 shows that the trend of spot size variation caused by FO changes as calculated according to Eq. (1), well fits with the observed trends of our experimental measurements (residual porosity, hardness and Al loss). Note that, we did not display the spot size values on the related axis because the beam spot size must be considered qualitatively since the coefficients of Eq. (1) change when using different beam currents. Actually, in Wadea et al. [33] it is not defined at which beam current the given coefficients are associated. However, according to the authors' opinion, Fig. 6 is a useful way to relate the effect of FO variations to the resulting material.

A wider electron beam spot size generates a larger melt pool size, and consequently, the energy input delivered is distributed on a more extensive area, thus lowering the local energy that reaches the powder bed. So the FO can play a fundamental role in generating a homogenous

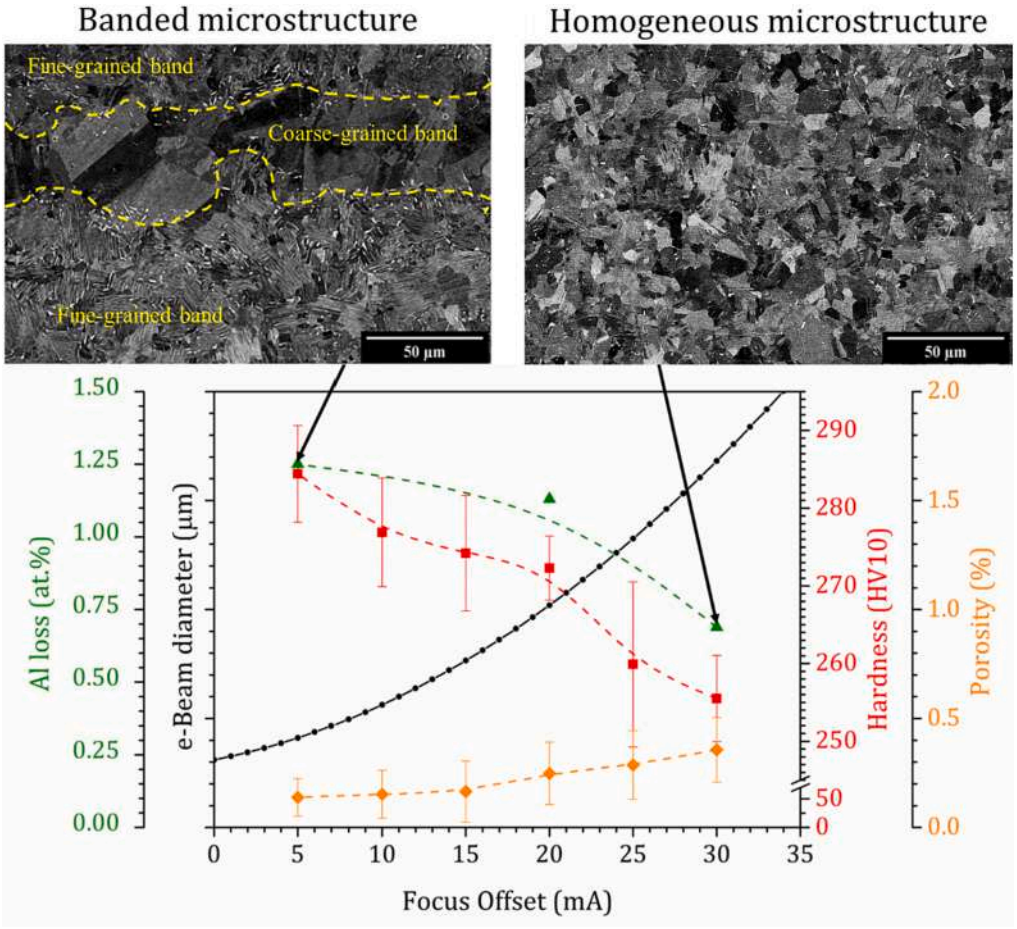

Fig. 6. Representation of the variation of the electron beam spot size (in black), Al loss (in green), hardness (in red), and porosity (in orange) with the FO. In addition, the microstructural features are shown. (For interpretation of the references to colour in this figure legend, the reader is referred to the web version of this article.)

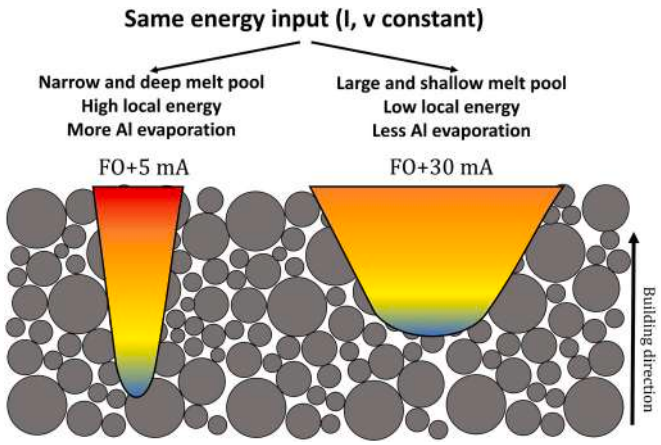

Fig. 7. Schematic illustration of shape and size of the melt pool with respect to focus offset in the EB-PBF process.

microstructure, mitigating the occurrence of a banded microstructure. A schematic illustration is presented in Fig. 7 showing the Gaussian beam and how it affects the melt pool size and, consequently, the Al evaporation.

Actually, the initial homogenous microstructure is a fundamental target for γ-TiAl based components since an inhomogeneous microstructure will result in undesirable and not uniform mechanical properties [48]. Moreover, the inhomogeneous microstructure cannot be homogenized through simple heat treatments, but will require high-temperature annealing followed by oil quenching [13]. This might induce cracks and metastable transformation unsuitable for industrial applications, especially for large components.

The parabolic trend of the spot size with respect to the FO explains the reason why the FO_{+15} and FO_{+20} still have a banded microstructure being more similar to FO_{+5} than FO_{+30}. In fact, going far from the minimum of the parabolic curve, the effect of increasing FO of the same quantity produces a wider spot size. Thus, FO_{+30} was revealed to be a condition that was successful for having homogeneous microstructure, with just a slight increase of spherical porosity without the presence of LoF.

3.2. Microstructural evolution under heat treatments

The heat treatments are mandatory for γ-TiAl-based components in order to reach the desired mechanical properties. For this reason, the influence of heat treatment on the sample FO_{+5} composed of a banded microstructure and the sample FO_{+30} with homogenous microstructure was investigated.

The heat treatment consisted of annealing at 1310 °C for 2 h, followed by cooling to room temperature at about 125 °C/min, as reported in previous works on Ti-48Al-2Cr-2Nb material which was processed by EB-PBF [13,19]. The temperature was chosen to bring the material to the $\alpha + \gamma$ phase-field region, thus obtaining a duplex microstructure after cooling. The same temperature was applied intentionally for both conditions (FO_{+5} and FO_{+30}) despite the different overall chemistry since the aim is not to reach a target microstructure after heat treatment, but to compare the microstructural homogeneity.

Fig. 8 shows the microstructures of the samples heat-treated at 1310 °C for 2 h for sample FO_{+5} (Fig. 8.a and b) and sample FO_{+30} (Fig. 8.c and d). The sample FO_{+5} presented wide lamellar colonies formed from the previous fine grains duplex γ/α_2 bands. These zones of the sample are the weakest point of the microstructure, leading to poor mechanical properties, as reported in the works of Todai et al. [24,26].

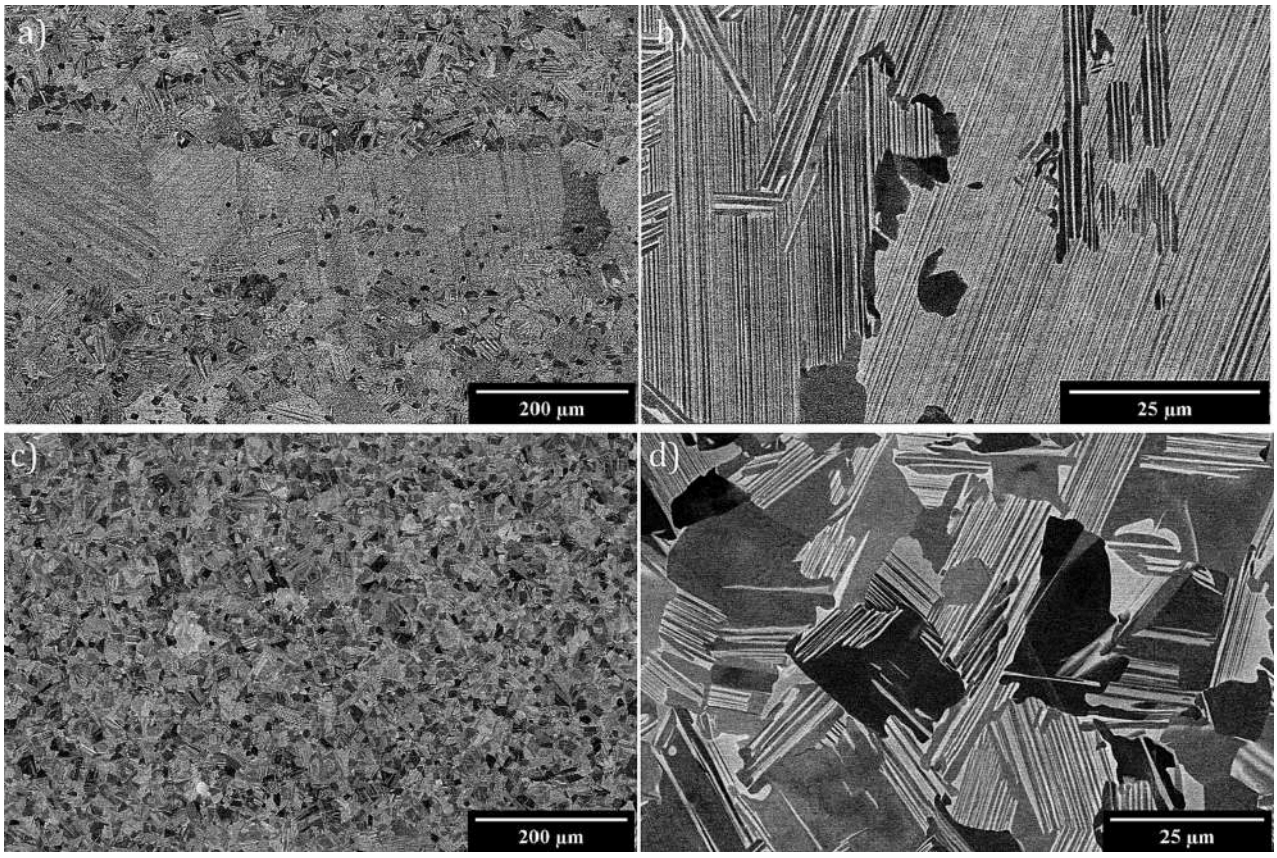

Fig. 8. a-b) SEM-BSE images of the heat-treated sample FO_{+5} at different magnifications; c-d) SEM-BSE images of the heat-treated sample FO_{+30} at different magnifications. Note that the heat treatment was performed at 1310 °C for 2 h, followed by a cooling rate of around 125 °C/min.

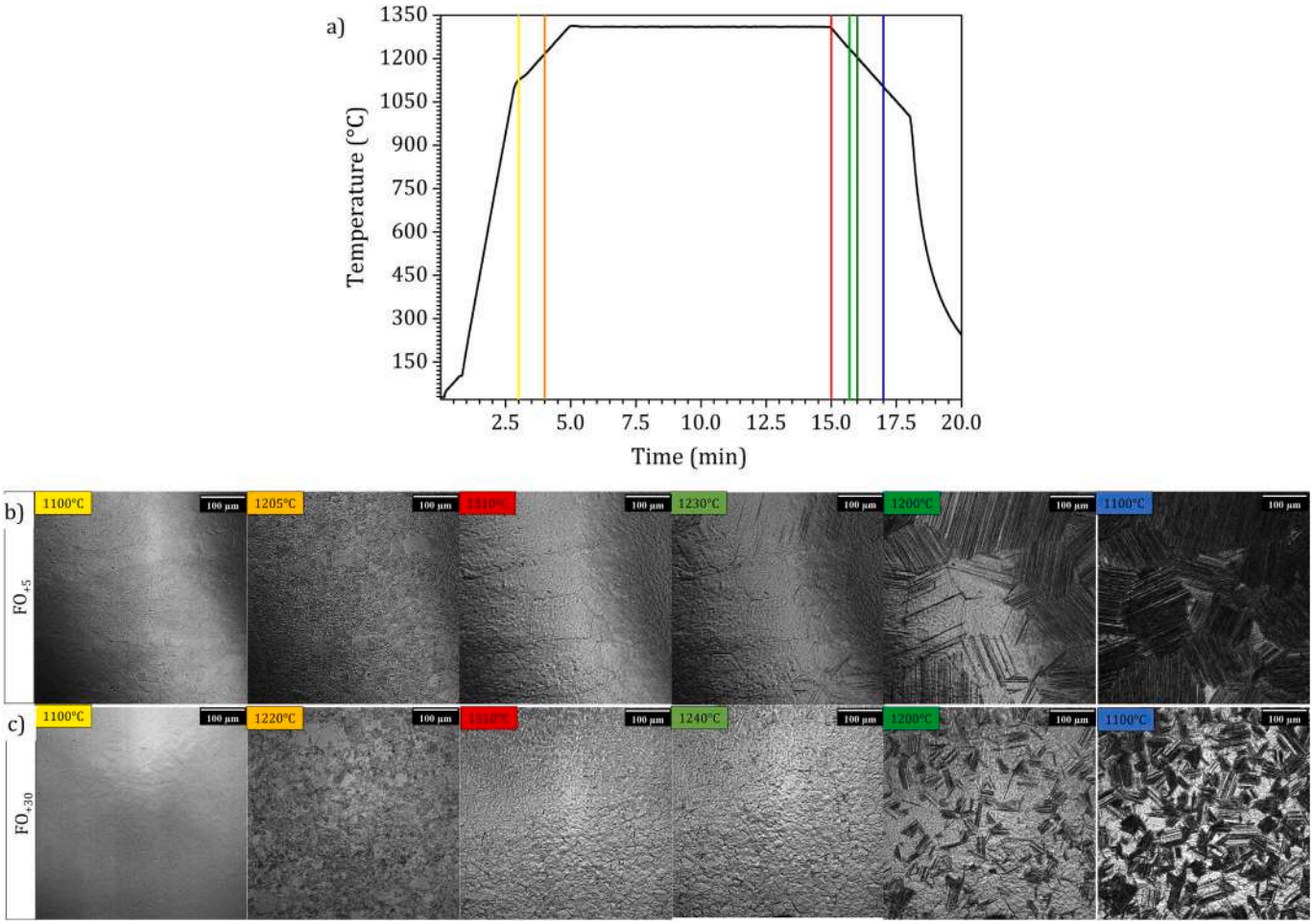

Fig. 9. LSCM results: a) temperature profile of the heat treatment: in b) images of the microstructure evolution for sample FO_{+5} c); images of the microstructure evolution for sample FO_{+30}. Note that the lines in a) point out where the microstructures at different temperatures were taken (see text).

On the contrary, the heat-treated sample FO_{+30} resulted in a more homogeneously duplex microstructure. The content of the lamellar phase was inferior because of the higher T_α with respect to FO_{+5}, but what was more important, the lamellar colonies were homogeneously distributed within the material (Fig. 8.c and d). If required by the application, the lamellar content can be increased by selecting a higher temperature for the heat treatment. This means, the microstructure can be tuned for the desired mechanical properties without risking the formation of large lamellar bands.

In order to directly observe the microstructure evolution during the heat treatment, LSCM analysis was performed. This technique allows video-recording of microstructural changes which occur with increasing of temperature. With LSCM, not only the different temperatures for the phase transformations due to the different Al-loss can be seen, but especially it was detected that the transformations appear contemporary and homogeneously in the sample with FO_{+30}, while take place at different times and temperatures for different zones of the sample processed with FO_{+5}. Microstructure images were extracted from the video recorded during the analysis at different temperatures, as pointed out by the lines in Fig. 9.a. In the supplementary data, the complete video of the measurement is available.

For sample FO_{+5}, the γ dissolution in the α-phase starts to be visible at around 1205 °C (Fig. 9.b). The dissolution initiated from fine γ-grains and α_2/γ regions and finished in the coarse γ-grains band. At 1310 °C (Fig. 9.b), the α-grains appeared coarse with a maximum dimension of around 200 µm. The lamellar colonies of γ/α_2-phases started to form at the α-phase grain boundaries during the cooling at around 1230 °C, following the steps reported by Appel et al. [49]. In detail, the formation of γ and α_2 lamellae follow the sequence $\alpha \rightarrow \alpha + \gamma \rightarrow \alpha_2 + \gamma$ with the applied cooling rate (100 °C/min). For the formation of the γ-lamellae, the stacking fault of the hcp lattice of the α-phase is the essential initial step. Then the formation can be subdivided into three phenomena; i) lattice transformation, ii) diffusion processes to adjust the composition of the γ-phase, and iii) ordering of the tetragonal face-centered γ-phase.

For sample FO_{+30}, the γ dissolution in the α-phase started to be visible at around 1220 °C (Fig. 9.c). The higher temperature is consistent with the higher Al content of this sample with respect to the FO_{+5}. In this case, the dissolution was uniformly distributed in the overall investigated area. At 1310 °C, the microstructure mainly consisted of homogeneously dispersed α grain with a maximum dimension of 50 µm. For the FO_{+30} condition, the lamellar precipitation started at around 1240 °C, so about 10 °C degrees higher when compared to the FO_{+5} state, again in agreement with the overall higher Al content.

For sample FO_{+5}, almost all the α-phase was transformed in lamellar grains of γ and α_2-phase at 1100 °C, while only a few regions remained γ-phase at the grain boundaries at room temperature. On the contrary, for the sample FO_{+30}, the final microstructure (below 1100 °C) appeared homogeneously duplex.

Therefore, the Al-depleted regions were characterized by early growth of the α-phase, which could grow enormously in the fine duplex bands locked only by the coarse γ-phase bands, which are the Al-rich regions. On the other hand, a homogeneous microstructure led to homogeneous nucleation of α-phase and uniform grain growth within the material.

4. Conclusions

An approach to contain the Al-loss typical of the EB-PBF process for intermetallic γ-TiAl components is to minimize the energy level of the process parameter for the production. However, there is a limit to such kind of approach because minimizing the beam current or increasing the beam speed, or increasing the line offset will, at a certain point, turn in not being able to have a completely dense material, but some process-induced porosity, the so-called lack-of-fusion defects, starts to form.

In this paper, the FO parameter is revealed to be another key parameter that can be optimized for generating a homogenous microstructure in an engineering Ti-48Al-2Cr-2Nb alloy because modifying the spot size can contribute to lower the energy level delivered in the powder bed.

The following conclusions can be drawn from the present study:

1) The increment of the FO mitigated the Al-loss as demonstrated by TMA and XRF analyses and a FO of 30 mA produced a homogenous microstructure.
2) Among the explored FOs, the porosity slightly increased with the FO increment. The porosity level was below 0.5 % for all the conditions, and what is more important, the investigations reveal only gas porosity defects, while no LoF defects were detected.

For the first time, to the authors' knowledge, in this work the microstructural evolution and phase transformations of a Ti-48Al-2Cr-2Nb alloy was recorded by means of LSCM analysis. The LSCM analysis revealed the phase transition $\alpha_2 + \gamma \rightarrow \alpha + \gamma$ during heating at different temperatures for the FO_{+5} and the FO_{+30} conditions. The growth of the α-phase became visible at 1205 °C and 1220 °C for FO_5 and $FO + 30$, respectively. For the FO_{+5} condition, the α-phase nucleates from the α_2/γ duplex band. Moreover, for this condition, the α-phase reached larger sizes than the FO_{+30} condition. During cooling, for the FO_{+30}, the lamellar formation started at a higher temperature (1240 °C) than the FO_5 (1230 °C). This resulted in a banded microstructure with large lamellar colonies for the FO_{+5} state, while the FO_{+30} state exhibited a homogenous finer duplex microstructure.

Supplementary data to this article can be found online at https://doi.org/10.1016/j.jmapro.2023.01.061.

Declaration of competing interest

The authors declare that they have no known competing financial interests or personal relationships that could have appeared to influence the work reported in this paper.

Acknowledgment

This project has received funding from the Clean Sky 2 Joint Undertaking under the European Union's Horizon 2020 research and innovation program under grant agreement No. 821274. The authors want to acknowledge also the Integrated Additive Manufacturing Centre at Politecnico di Torino (IAM @PoliTo), where the specimens were produced.

References

[1] Appel F, Oehring M, Wagner R. Novel design concepts for gamma-base titanium aluminide alloys. Intermetallics 2000;8:1283–312. https://doi.org/10.1016/S0966-9795(00)00036-4.
[2] Clemens BH, Mayer S, Schwaighofer E, Werner R, Gaitze A. In: Design, processing, microstructure, properties, and applications of advanced intermetallic TiAl alloys; 2013. p. 191–215. https://doi.org/10.1002/adem.201200231.
[3] Appel F, Clemens H, Fischer FD. Modeling concepts for intermetallic titanium aluminides. Prog Mater Sci 2016;81:55–124. https://doi.org/10.1016/j.pmatsci.2016.01.001.
[4] Dimiduk DM. Gamma titanium aluminide alloys - an assessment within the competition of aerospace structural materials. Mater Sci Eng A 1999;263:281–8. https://doi.org/10.1016/s0921-5093(98)01158-7.
[5] Liu Z, Yin G, Zhu X, Zhou Q. Microstructure, texture and tensile properties as a function of laser power of Ti48Al2Cr2Nb5Ta alloy prepared by laser additive manufacturing. J Manuf Process 2022;73:624–32. https://doi.org/10.1016/j.jmapro.2021.11.039.
[6] Soliman HA, Yakout M, Elbestawi M. Laser powder bed fusion of titanium aluminides using sequential thermal scanning strategy. J Manuf Process 2022;83:438–57. https://doi.org/10.1016/j.jmapro.2022.09.014.
[7] Mitra R, Wanhill RJH. Aerospace materials and material technologies, volume 1: aerospace material technologies. Aerosp Mater Mater Technol 2017;1:586. https://doi.org/10.1007/978-981-10-2134-3.
[8] Bewlay BP, Nag S, Suzuki A, Weimer MJ. TiAl alloys in commercial aircraft engines. Mater High Temp 2016;33:549–59. https://doi.org/10.1080/09603409.2016.1183068.
[9] Baudana G. γ-Titanium aluminide alloys for aircraft and automotive engine components applications processed by electron beam melting. 2018.
[10] Burtscher M, Klein T, Lindemann J, Lehmann O, Fellmann H, Güther V, Clemens H, Mayer S. An advanced tial alloy for high-performance racing applications. Materials (Basel) 2020;13:1–14. https://doi.org/10.3390/ma13214720.
[11] Güther V, Allen M, Klose J, Clemens H. Metallurgical processing of titanium aluminides on industrial scale. Intermetallics 2018;103:12–22. https://doi.org/10.1016/j.intermet.2018.09.006.
[12] Wu X. In: Review of alloy and process development of TiAl alloys. 14; 2006. p. 1114–22. https://doi.org/10.1016/j.intermet.2005.10.019.
[13] Wartbichler R, Ghibaudo C, Rizza G, Galati M, Iuliano L, Biamino S, Ugues D, Allen M, Hirn S, Clemens H, Mayer S. In: On the formation mechanism of banded microstructures in electron beam melted Ti-48Al-2Cr-2Nb and the utilization of heat treatments as remedial action; 2021. p. 2101199. https://doi.org/10.1002/adem.202101199.
[14] Zhou J, Li H, Yu Y, Li Y, Qian Y, Firouzian K, Lin F. Research on aluminum component change and phase transformation of TiAl-based alloy in electron beam selective melting process under multiple scan. Intermetallics 2019;113:106575. https://doi.org/10.1016/j.intermet.2019.106575.
[15] Recina V, Lundstrom D, Karlsson B. Tensile, creep, and low-cycle fatigue behavior of a cast g -TiAl – based alloy for gas turbine applications. Metall Mater Trans A 2002;33:2869–81.
[16] Kim YW, Dimiduk DM. Progress in the understanding of gamma titanium aluminides. Jom 1991;43:40–7. https://doi.org/10.1007/BF03221103.
[17] Fashu S, Lototskyy M, Davids MW, Pickering L, Linkov V, Tai S, Renheng T, Fangming X, Fursikov PV, Tarasov BP. A review on crucibles for induction melting of titanium alloys. Mater Des 2020;186:108295. https://doi.org/10.1016/j.matdes.2019.108295.
[18] Schwerdtfeger J, Körner C. Intermetallics selective electron beam melting of Tie48Ale2Nbe2Cr: microstructure and aluminium loss. Intermetallics 2014;49:29–35. https://doi.org/10.1016/j.intermet.2014.01.004.
[19] Biamino S, Penna A, Ackelid U, Sabbadini S, Tassa O, Fino P, Pavese M, Gennaro P, Badini C. Electron beam melting of Ti-48Al-2Cr-2Nb alloy: microstructure and mechanical properties investigation. Intermetallics 2011;19:776–81. https://doi.org/10.1016/j.intermet.2010.11.017.
[20] Murr LE, Gaytan SM, Ceylan A, Martinez E, Martinez JL, Hernandez DH, Machado BI, Ramirez DA, Medina F, Collins S, Wicker RB. Characterization of titanium aluminide alloy components fabricated by additive manufacturing using electron beam melting. Acta Mater 2010;58:1887–94. https://doi.org/10.1016/j.actamat.2009.11.032.
[21] Hernandez J, Murr LE, Gaytan SM, Martinez E, Medina F, Wicker RB. Microstructures for two-phase gamma titanium aluminide fabricated by electron beam melting. Metallogr Microstruct Anal 2012;1:14–27. https://doi.org/10.1007/s13632-011-0001-9.
[22] Murr LE, Gaytan SM. Electron beam melting. Elsevier; 2014. https://doi.org/10.1016/B978-0-08-096532-1.01004-9.
[23] Körner C. Additive manufacturing of metallic components by selective electron beam melting - a review. Int. Mater. Rev. 2016;61:361–77. https://doi.org/10.1080/09506608.2016.1176289.
[24] Cho K, Kobayashi R, Oh JY, Yasuda HY, Todai M, Nakano T, Ikeda A, Ueda M, Takeyama M. Influence of unique layered microstructure on fatigue properties of Ti-48Al-2Cr-2Nb alloys fabricated by electron beam melting. Intermetallics. 2018;95:1–10. https://doi.org/10.1016/j.intermet.2018.01.009.
[25] Klassen A, Forster VE, Juechter V, Körner C. Numerical simulation of multi-component evaporation during selective electron beam melting of TiAl. J Mater Process Technol 2017;247:280–8. https://doi.org/10.1016/j.jmatprotec.2017.04.016.
[26] Todai M, Nakano T, Liu T, Yasuda HY, Hagihara K, Cho K, Ueda M, Takeyama M. Effect of building direction on the microstructure and tensile properties of Ti-48Al-2Cr-2Nb alloy additively manufactured by electron beam melting. Addit Manuf 2017;13:61–70. https://doi.org/10.1016/j.addma.2016.11.001.
[27] Polonsky AT, Echlin MP, Lenthe WC, Dehoff RR, Kirka MM, Pollock TM. Defects and 3D structural inhomogeneity in electron beam additively manufactured inconel 718. Mater Charact 2018;143:171–81. https://doi.org/10.1016/j.matchar.2018.02.020.
[28] Zhao X, Dadbakhsh S, Rashid A. Contouring strategies to improve the tensile properties and quality of EBM printed inconel 625 parts. J Manuf Process 2021;62:418–29. https://doi.org/10.1016/j.jmapro.2020.12.007.
[29] Szymczyk-Ziółkowska P, Ziółkowski G, Hoppe V, Rusińska M, Kobiela K, Madeja M, Dziedzic R, Junka A, Detyna J. Improved quality and functional properties of Ti-

6Al-4V ELI alloy for personalized orthopedic implants fabrication with EBM process. J Manuf Process 2022;76:175–94. https://doi.org/10.1016/j.jmapro.2022.02.011.
[30] Ghibaudo C, Rizza G, Marchese G, Galati M, Iuliano L, Ugues D, Biamino S. A comparison of different approches to study the porosity and surfacedefects for Electron Beam Melting. In: Euro PM 2021, Congr. Exhib; 2021.
[31] Mohammad A, Al-ahmari AM, Mohammed MK. In: Effect of melt parameters on density and surface roughness in electron beam melting of gamma titanium aluminide alloy. 3; 2017. p. 474–85. https://doi.org/10.1108/RPJ-12-2014-0187.
[32] Cooke S, Ahmadi K, Willerth S, Herring R. Metal additive manufacturing: technology, metallurgy and modelling. J Manuf Process 2020;57:978–1003. https://doi.org/10.1016/j.jmapro.2020.07.025.
[33] Wadea A, Khan MMuneer, Abdulrahman A-A. Evaluation of support structure removability for additively manufactured Ti6Al4V overhangs via electron beam melting. Metals (Basel) 2019;9.
[34] Karimi P, Sadeghi E, Ålgårdh J, Andersson J. EBM-manufactured single tracks of alloy 718: influence of energy input and focus offset on geometrical and microstructural characteristics. Mater Charact 2019;148:88–99. https://doi.org/10.1016/j.matchar.2018.11.033.
[35] Lee HJ, Kim HK, Hong HU, Lee BS. Influence of the focus offset on the defects, microstructure, and mechanical properties of an inconel 718 superalloy fabricated by electron beam additive manufacturing. J Alloys Compd 2019;781:842–56. https://doi.org/10.1016/j.jallcom.2018.12.070.
[36] Luo Y, Ye H, Du C, Xu H. Influence of focusing thermal effect upon AZ91D magnesium alloy weld during vacuum electron beam welding. Vacuum 2012;86:1262–7. https://doi.org/10.1016/j.vacuum.2011.11.011.
[37] Lin Z, Dabakhsh S, Rashid A. Developing processing windows for powder pre-heating in electron beam melting. J Manuf Process 2022;83:180–91. https://doi.org/10.1016/j.jmapro.2022.08.063.
[38] Germain L, Dey SR, Humbert M, Gey N. Determination of parent orientation maps in advanced titanium-based alloys. J Microsc 2007;227:284–91. https://doi.org/10.1111/j.1365-2818.2007.01812.x.
[39] Dey SR, Bouzy E, Hazotte A. EBSD characterisation of massive γ nucleation and growth in a TiAl-based alloy. Intermetallics 2006;14:444–9. https://doi.org/10.1016/j.intermet.2005.08.010.
[40] Reith M, Franke M, Schloffer M, Körner C. Processing 4th generation titanium aluminides via electron beam based additive manufacturing – characterization of microstructure and mechanical properties. Materialia 2020;14:100902. https://doi.org/10.1016/j.mtla.2020.100902.
[41] Baudana G, Biamino S, Klöden B, Kirchner A, Weißgärber T, Kieback B, Pavese M, Ugues D, Fino P, Badini C. Electron beam melting of Ti-48Al-2Nb-0.7Cr-0.3Si: feasibility investigation. Intermetallics 2016;73:43–9. https://doi.org/10.1016/j.intermet.2016.03.001.
[42] Juechter V, Franke MM, Merenda T, Stich A, Körner C, Singer RF. Additive manufacturing of ti-45Al-4Nb-C by selective electron beam melting for automotive applications. Addit Manuf 2018;22:118–26. https://doi.org/10.1016/j.addma.2018.05.008.
[43] Huang K, Logé RE. A review of dynamic recrystallization phenomena in metallic materials. Mater Des 2016;111:548–74. https://doi.org/10.1016/j.matdes.2016.09.012.
[44] Smith CS, Rohrer GS. Grains, Phases, and Interfaces: An interpretation of Microstrucure. 1948. https://doi.org/10.1007/s11661-010-0215-5.
[45] Schloffer M, Iqbal F, Gabrisch H, Schwaighofer E, Schimansky FP, Mayer S, Stark A, Lippmann T, Göken M, Pyczak F, Clemens H. Microstructure development and hardness of a powder metallurgical multi phase γ-TiAl based alloy. Intermetallics 2012;22:231–40. https://doi.org/10.1016/j.intermet.2011.11.015.
[46] Juechter V, Franke MM, Merenda T, Stich A, Körner C, Singer RF. Additive manufacturing of ti-45Al-4Nb-C by selective electron beam melting for automotive applications. Addit Manuf 2018;22:118–26. https://doi.org/10.1016/j.addma.2018.05.008.
[47] Terner M, Biamino S, Ugues D, Sabbadini S, Fino P, Pavese M, Badini C. Phase transitions assessment on γ-TiAl by thermo mechanical analysis. Intermetallics. 2013;37:7–10. https://doi.org/10.1016/j.intermet.2013.01.019.
[48] Lin B, Chen W, Yang Y, Wu F, Li Z. Anisotropy of microstructure and tensile properties of Ti–48Al–2Cr–2Nb fabricated by electron beam melting. J Alloys Compd 2020;830:154684. https://doi.org/10.1016/j.jallcom.2020.154684.
[49] Appel F, Paul DH, Oehring M. Gamma Titanium Aluminide Alloys. 2011.